Research Square

Preprints are preliminary reports that have not undergone peer review.
They should not be considered conclusive, used to inform clinical practice,
or referenced by the media as validated information.

Pocket-Dependent Quantum-Oscillation Phases and Multiband Magnetotransport in LaSb

Kwan-Young Lee
Kyung Hee University
Wonhyuk Shon
Korea Atomic Energy Research Institute
Kornelius Nielsch
Leibniz Institute for Solid State and Materials Research
Nicolas Perez
Leibniz Institute for Solid State and Materials Research
Jong-Soo Rhyee
jsrhyee@khu.ac.kr

Kyung Hee University

Research Article

Keywords:

Posted Date: November 26th, 2026

DOI: https://doi.org/10.21203/rs.3.rs-11691709/v1

License: This work is licensed under a Creative Commons Attribution 4.0 International License.
Read Full License

Additional Declarations: No competing interests reported.

Pocket-Dependent Quantum-Oscillation Phases and Multiband Magnetotransport in LaSb

Kwan-Young Lee[1,†], Wonhyuk Shon[2,†], Kornelius Nielsch[3], Nicolas Perez[3], Jong-Soo Rhyee[1,*]

[1]Department of Applied Physics, Institute of Natural Sciences, Kyung Hee University, Yongin 17104, Republic of Korea

[2]Korea Atomic Energy Research Institute, Daejeon 34057, Republic of Korea

[3]Leibniz Institute for Solid State and Materials Research IFW Dresden, Dresden 01069, Germany

[†]These authors contributed equally to this work.

[*]Corresponding author: Jong-Soo Rhyee; e-mail: jsrhyee@khu.ac.kr

Abstract

LaSb is a compensated semimetal that exhibits non-saturating extreme magnetoresistance (XMR), yet the microscopic origin of its transport behavior remains debated. We report a combined magnetotransport and quantum-oscillation study on high-quality LaSb single crystals to examine the roles of carrier compensation, mobility, and pocket-dependent electronic structure. The data reveal a compensated multiband state with high mobility, a field-induced resistivity upturn, a low-temperature plateau, and pronounced angular magnetoresistance anisotropy. Quantum oscillations reveal three principal frequency branches, assigned by comparison with established LaSb Fermi surfaces to an X-centered electron-pocket family and two Γ-centered hole pockets. Landau-fan analysis yields distinct orbit-dependent phase offsets: the α electron orbit and β hole orbit are compatible with trivial phases, whereas the γ hole orbit is compatible with a nontrivial Berry-phase contribution under the adopted three-dimensional phase convention. Multicarrier conductivity fits improve as additional effective Drude components are included beyond a minimal electron–hole description, highlighting the role of pocket-dependent transport weights despite near overall compensation. These results link the XMR state to the cooperative effects of near compensation, high mobility, and anisotropic multiband transport, while identifying pocket-dependent phase signatures within the same electronic system.

Keywords: LaSb; extreme magnetoresistance; quantum oscillations; multiband transport; Berry phase

1 Introduction

Extremely large, non-saturating extreme magnetoresistance (XMR) in nonmagnetic semimetals has attracted sustained interest because it provides a sensitive probe of the interplay between electronic structure and charge transport[1–9]. In several material classes, including WTe_2, Cd_3As_2, and the TaAs family, XMR has been discussed in connection with electron–hole compensation, ultrahigh carrier mobility, suppressed backscattering, and nontrivial band topology[3;10–16]. Beyond its fundamental significance, this phenomenon is also relevant to magnetic sensing and other electronic applications that benefit from large field-dependent transport responses.

Rare-earth monopnictides LaX (X = P, As, Sb, Bi) have emerged as an especially useful platform for investigating XMR because they combine simple crystal symmetry with rich multiband electronic structure[17–22]. Among them, LaSb has been widely regarded as a prototypical compensated semimetal exhibiting near-quadratic, non-saturating magnetoresistance that can reach 10^5–10^6% at low temperature and high magnetic field[1;2;19]. Despite extensive study, however, the microscopic origin of XMR in LaSb remains unsettled.

A common interpretation attributes the large magnetoresistance of LaSb to near-perfect electron–hole compensation, analogous to the mechanism proposed for other compensated semimetals[2;18;20;23;24]. Within this picture, large, non-saturating magnetoresistance follows naturally from near equality of the total electron and hole densities in the presence of high carrier mobility. However, compensation alone may not provide a complete description of the transport phenomenology. In particular, the field-induced resistivity upturn, low-temperature plateau, nonlinear Hall response, and pronounced angular anisotropy suggest that the transport state is governed by multiple carrier channels with distinct mobilities and orbital characters[19;25–27]. These features raise the possibility that the XMR state in LaSb reflects not merely a compensated two-carrier metal, but a more intricate multiband system in which pocket-dependent transport contributions evolve strongly with temperature and field.

The topological character of LaSb is likewise under debate. Theoretical and experimental investigations have reached differing conclusions on whether LaSb is topologically trivial or hosts band inversion and topological surface states[28–31]. For example, first-principle calculations based on the conventional PBE (Perdew-Burke-Ernzerhof) functional predict a band inversion at the X point, suggesting a nontrivial topological character, whereas calculations using the modified Becke-Johnson (mBJ) potential remove the band inversion and instead predict a topologically trivial electronic structure[20]. Experimental investigations have also produced conflicting conclusions regarding the topology of LaSb. Surface-sensitive VUV-ARPES measurements reported Dirac-like dispersions that were interpreted as possible topological surface states[28], whereas bulk-sensitive soft-X-ray ARPES found no band inversion and classified LaSb as a topologically trivial semimetal[29]. These contrasting observations motivate a pocket-

resolved analysis of quantum-oscillation phases alongside the existing evidence on bulk and surface electronic structure.

Quantum oscillation measurements are particularly well suited for this purpose because they provide direct access to extremal Fermi-surface areas, carrier-pocket assignment, and oscillation phase. When combined with Hall analysis and multicarrier conductivity modeling, they offer a means of distinguishing the relative roles of compensation, mobility, Fermi-surface anisotropy, and Berry-phase-related topology in governing XMR. In LaSb, such a combined analysis is especially important because the transport response appears to involve more complexity than is captured by a minimal two-band description.

In this work, we present a comprehensive magnetotransport and quantum-oscillation study of high-quality LaSb single crystals. We show that the material exhibits a compensated multiband state with high carrier mobility, field-induced resistivity upturn and plateau behavior, and strongly anisotropic angular magnetoresistance. Quantum oscillations reveal three principal branches, associated with the α electron-pocket family and the β and γ hole pockets using the nomenclature of Han et al.[19]. Landau-level fan diagrams reveal pocket-dependent phase signatures: the α and β orbits are compatible with trivial phases, while the γ orbit is compatible with a nontrivial Berry-phase contribution. In parallel, including additional effective components in the multicarrier conductivity model improves the description of the measured transport, even though the low-temperature state remains close to overall electron–hole compensation. These results connect the XMR of LaSb with compensation, high mobility, and anisotropic multiband transport, and place the distinct orbit-phase signatures in this broader transport context.

2 Experimental Details

Single crystals of LaSb were grown by a Sn-flux method using a high-frequency induction furnace. High-purity elemental La (99.9%), Sb (99.999%), and Sn (99.99%) were mixed in the desired molar ratio, loaded into ampoules, and sealed under vacuum below 10^{-5} Torr[1;19]. The sealed ampoules were heated to 700 °C at a rate of 50 °C h^{-1}, held at that temperature for 30 h, and then slowly cooled to 470 °C at 1 °C h^{-1}. The samples were subsequently annealed at 470 °C for 200 h. After annealing, the excess Sn flux was removed immediately by centrifugation. Plate-like single crystals with typical dimensions of approximately $5 \times 5 \times 1$ mm^3 were mechanically separated for structural, transport, and magnetic measurements.

The crystal structure and phase purity were characterized by x-ray diffraction (XRD) using Cu Kα radiation (Bruker D8 Advance, Germany). XRD patterns were collected from several representative crystals to confirm the crystallographic orientation and the absence of detectable impurity phases.

The surface morphology and elemental distribution were examined by scanning electron mi-

croscopy and energy-dispersive X-ray spectroscopy using a ZEISS SIGMA 300 system. The measurements were performed with an electron high tension of 10.00 kV. The SEM image, elemental maps of La, Sb, and Sn, and the corresponding quantitative compositional analysis are provided in Fig. S1 and Table S1 of the Supplementary Material. The results confirm a La:Sb atomic ratio of approximately 1:1 with no appreciable residual Sn contamination from the flux-growth process.

Electrical transport and magnetic measurements were carried out in a Physical Property Measurement System (PPMS DynaCool 14 T, Quantum Design, USA). Longitudinal resistivity and Hall resistivity were measured using a standard four-probe configuration with the electrical transport option. The magnetic field was applied up to 14 T. For Hall measurements, the transverse voltage was antisymmetrized with respect to magnetic-field reversal to remove the longitudinal resistivity contribution arising from contact misalignment, while the longitudinal resistivity was symmetrized. Magnetization measurements were performed using the vibrating sample magnetometer option of the PPMS.

Angular-dependent magnetoresistance measurements were conducted by rotating the magnetic field with respect to the current direction and crystallographic axes using two rotation geometries, denoted by θ and ϕ. Shubnikov–de Haas oscillations were extracted from the field-dependent transport data after subtraction of a smooth background, and de Haas–van Alphen oscillations were obtained from the magnetization data in an analogous manner. The quantum-oscillation frequencies were determined by fast Fourier transform analysis as a function of inverse magnetic field.

3 Results and Discussion

3.1 Magnetotransport properties of LaSb

Figure 1(a) shows the x-ray diffraction pattern of the LaSb single crystal. The sharp (200) and (400) reflections can be indexed to the rock-salt cubic structure with space group $Fm\bar{3}m$, confirming the high crystalline quality and preferred orientation along the (100) direction. No detectable impurity peaks are observed except for minor reflections attributed to the sample holder. The extracted lattice parameter is consistent with previous reports for LaSb, indicating that the synthesized crystals are phase pure and structurally well ordered.

The temperature dependence of the longitudinal resistivity $\rho_{xx}(T)$ under transverse magnetic field is presented in Fig. 1(b). At zero field, LaSb exhibits good metallic behavior, with ρ_{xx} decreasing monotonically upon cooling and reaching a residual resistivity of approximately 1.3 $\mu\Omega$cm at 2 K. Upon application of magnetic field, the resistivity develops a pronounced upturn below a characteristic temperature T_m, followed by a low-temperature plateau. This field-induced metal-to-insulator-like crossover and plateau behavior are characteristic features

of extreme magnetoresistance (XMR) semimetals and are commonly associated with compensated multicarrier transport under strong orbital magnetoresistance[1;10;18;19;32;33].

The derivative $d\rho_{xx}/dT$ in Fig. 1(c) highlights the temperature intervals over which the field-induced upturn develops. At finite field, the negative derivative in the upturn region contrasts with the metallic zero-field response, while the small temperature variation at the lowest temperatures reflects the approach to the plateau. To compare the shapes of the resistivity curves independently of their field-dependent magnitudes, Fig. 1(d) shows the normalized change

$$R_{\mathrm{N}}(T,B) = \frac{\rho_{xx}(T,B) - \rho_{xx}(2\ \mathrm{K},B)}{\rho_{xx}(2\ \mathrm{K},B)}.$$

The reference resistivity is taken at 2 K separately for each field. The finite-field curves remain close to their plateau reference at low temperature, decrease across the intermediate-temperature interval, and become more clearly separated above approximately 50 K. The shaded intervals in Fig. 1(d), separated near 12 and 50 K, highlight these changes in curve shape rather than independently determined phase boundaries. This comparison provides a common temperature scale for the resistivity, Hall, and angular-magnetoresistance responses discussed below.

Further insight is obtained from the Hall resistivity $\rho_{xy}(H)$, shown in Fig. 2. At low temperature, $\rho_{xy}(H)$ is strongly nonlinear, immediately indicating that the transport cannot be described within a single-carrier approximation, as presented in Fig. 2(a). Instead, the Hall response reflects the simultaneous contribution of electron- and hole-like carriers with different mobilities. In a compensated multiband semimetal, the sign and curvature of the Hall resistivity are determined by the mobility-weighted balance of the various conductivity channels rather than by carrier density alone. The temperature-dependent evolution and sign reversal of $\rho_{xy}(H)$ therefore indicate a continuous rebalancing of the transport-active pockets, rather than a simple crossover between electron-dominated and hole-dominated conduction.

Figure 2(b) presents the magnetic-field dependence of the Hall resistivity, $\rho_{xy}(H)$, in the intermediate- and high-temperature range. Importantly, the Hall response remains distinctly nonlinear over the entire measured temperature window, indicating that the transport in LaSb cannot be reduced to a simple single-carrier description even at elevated temperatures. The persistence of Hall nonlinearity supports a multicarrier response over the measured temperature range. Together with the established electron and hole pockets of LaSb and the effective two-band analysis, this behavior is consistent with concurrent electron and hole contributions. This behavior is a characteristic signature of robust multiband transport and shows that thermal scattering does not eliminate the underlying complexity of the compensated semimetallic state.

Within a multicarrier framework, the Hall resistivity is determined by the field-dependent balance between carrier densities and mobilities of the individual transport channels. Therefore,

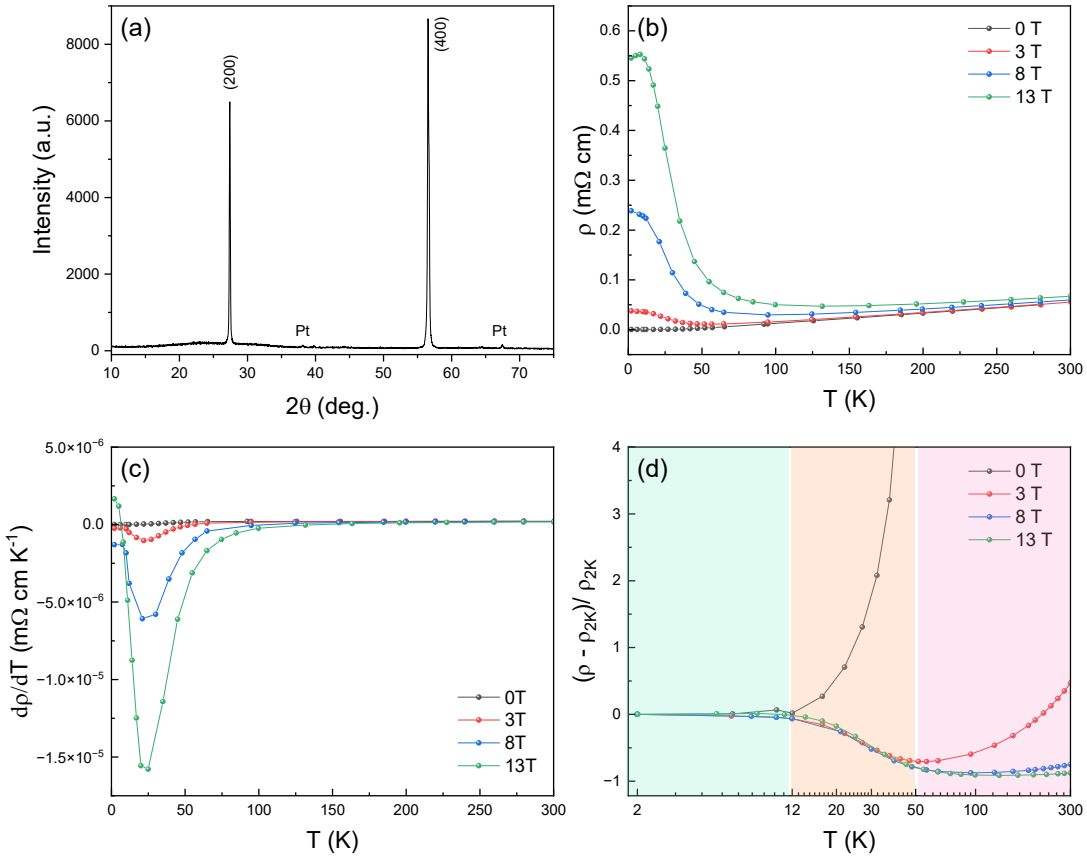

Fig. 1. (a) X-ray diffraction pattern of a LaSb single crystal. The dominant (200) and (400) reflections indicate the preferred (100) orientation of the rock-salt structure; minor peaks marked Pt originate from the sample holder. (b) Temperature-dependent longitudinal resistivity at transverse magnetic fields of 0, 3, 8, and 13 T. (c) Temperature derivative of the resistivity curves in (b). (d) Normalized resistivity change $[\rho_{xx}(T,B) - \rho_{xx}(2\ \mathrm{K},B)]/\rho_{xx}(2\ \mathrm{K},B)$, using a separate 2 K reference for each field, on a logarithmic temperature axis. Shading marks the approximate intervals 2–12 K, 12–50 K, and above 50 K and does not denote independently established phase boundaries.

the temperature evolution and sign change of $\rho_{xy}(H)$ should not be interpreted as a crossover to a high-temperature single-band regime, but rather as evidence for a continuous redistribution of the relative transport weights among several Fermi-surface pockets. In particular, the pronounced evolution in the vicinity of 40–50 K suggests that this temperature range marks a crossover in the effective multicarrier conduction, consistent with the anomalies observed in the longitudinal resistivity and angular-dependent magnetoresistance.

The carrier concentrations and Hall mobilities shown in Fig. 2(c) were extracted by simultaneously fitting the measured longitudinal and Hall resistivities using the standard semiclassical two-band Drude model. This analysis provides effective electron and hole transport parameters describing the dominant compensated transport. The two-band model provides effective parameters for the overall temperature evolution, while the multicarrier analysis in Section 3.4 examines the detailed low-temperature conductivity within the low-field interval displayed in Fig. 8. The electron mobility is strongly enhanced at low temperature and decreases rapidly upon warming, whereas the hole mobility varies more moderately. At the same time, the effective carrier densities also evolve with temperature, indicating that the Hall response is governed by a coupled renormalization of both mobility and transport-weighted carrier contribution. Because the Hall conductivity depends sensitively on these quantities, even moderate temperature-induced changes can strongly modify the curvature and sign of $\rho_{xy}(H)$ without destroying the compensated multiband character. The fact that the most rapid variation occurs below approximately 50 K further supports the conclusion that the XMR state in LaSb is stabilized by a delicate balance of multiple transport-active pockets with strongly temperature-dependent weights.

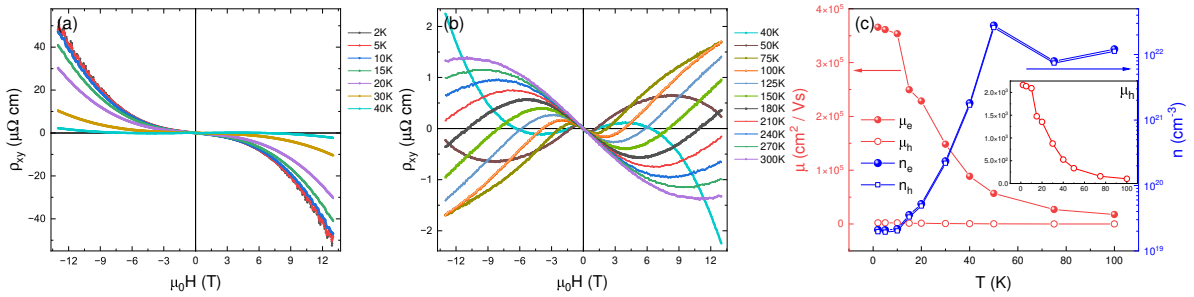

Fig. 2. Isothermal Hall resistivity for (a) 2–40 K and (b) 40–300 K. (c) Effective electron and hole mobilities μ_e and μ_h (red filled and open circles, left axis) and carrier densities n_e and n_h (blue filled circles and open squares, right logarithmic axis) for 2–100 K, obtained from simultaneous two-band fits to the longitudinal and Hall resistivities. The inset enlarges the temperature dependence of μ_h. Mobilities and densities are plotted in $\mathrm{cm}^2\,\mathrm{V}^{-1}\,\mathrm{s}^{-1}$ and cm^{-3}, respectively.

3.2 Angular-dependent magnetoresistance and anisotropic transport

The anisotropic nature of the XMR state was investigated through angular-dependent magnetoresistance (ADMR) measurements, with the measurement geometries for θ and φ rotations illustrated in Fig. 3(a). Representative field-dependent magnetoresistance curves are shown in Fig. 3(b) and Fig. 3(c). At 2 K and 13 T, the magnetoresistance exceeds $1.4 \times 10^5\%$ in the transverse configuration, consistent with the compensated high-mobility state inferred from the longitudinal and Hall transport data. Rotating the magnetic field toward the nearly longitudinal configuration strongly suppresses the MR. The full angular scans in Figs. 4 and 5 further reveal a smoother two-lobed response for the θ rotation and additional angular structure for the φ rotation.

In a conventional compensated semimetal, the positive magnetoresistance is generally attributed to the orbital response driven by the Lorentz force, and this contribution is expected to be progressively suppressed as the field is rotated toward the longitudinal configuration, $\mathbf{B} \parallel \mathbf{J}$[1;2;19]. An intrinsic decrease of the longitudinal resistance below its zero-field value would require a contribution beyond this positive orbital background.

In topological Dirac and Weyl semimetals, negative longitudinal magnetoresistance has been widely discussed as a transport signature of the Adler–Bell–Jackiw chiral anomaly, which arises from charge pumping between nodes of opposite chirality under parallel electric and magnetic fields[12;34]. In such a situation, the longitudinal conductivity acquires an additional positive contribution,

$$\Delta\sigma_{\text{chiral}} \propto B^2,$$

in the weak-field limit for $\mathbf{E} \parallel \mathbf{B}$, which manifests experimentally as a negative magnetoresistance[10;12]. This provides one possible framework for discussing the nearly longitudinal response in Figs. 3(b) and 3(c), without identifying its microscopic origin from the MR sign alone.

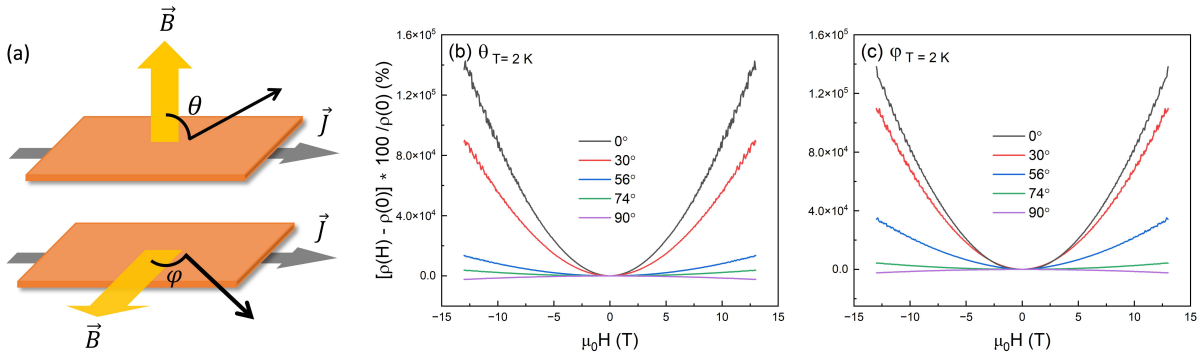

Fig. 3. (a) Schematics of the out-of-plane θ rotation and in-plane ϕ rotation relative to the current direction $\mathbf{J}$. Field-dependent magnetoresistance at $T = 2$ K for (b) θ and (c) ϕ rotations, measured at 0°, 30°, 56°, 74°, and 90° as indicated. Magnetoresistance is defined as $\text{MR} = 100\,[\rho_{xx}(B) - \rho_{xx}(0)]\,/\rho_{xx}(0)$, with $\rho_{xx}(0)$ the zero-field resistivity at the same temperature.

At the same time, caution is required because negative longitudinal magnetoresistance is not, by itself, definitive proof of the chiral anomaly. Similar behavior may also result from current jetting, conductivity fluctuations, weak-localization effects, or other geometric and extrinsic mechanisms[35]. Therefore, the present data are most appropriately interpreted as evidence consistent with, rather than uniquely demonstrating, chiral-anomaly-related transport. The angular selectivity motivates comparison with the pocket-dependent phase signatures discussed below, but does not establish that the longitudinal response and the oscillation phases have a common topological origin.

Figures 4 and 5 provide a detailed view of the temperature- and field-dependent evolution of the angular magnetoresistance (MR) in LaSb and reveal a highly anisotropic response that is strongly enhanced in the low-temperature, high-field regime. In the transverse configuration, the MR remains large and positive, reflecting the strong orbital response expected for a compensated semimetal with high carrier mobility[1;2;19]. By contrast, as the magnetic field is rotated toward the longitudinal geometry, where $\mathbf{B} \parallel \mathbf{J}$, the positive orbital contribution is progressively suppressed and a pronounced reduction of the MR emerges. In the φ-rotation geometry, the strongest suppression occurs around the nearly longitudinal direction. The angular profiles therefore reveal how the large transverse orbital response is reduced as the field approaches $\mathbf{B} \parallel \mathbf{J}$.

A useful phenomenological description separates the large positive orbital background from the strongly orientation-dependent longitudinal response. A chiral-anomaly contribution is one possible microscopic interpretation of the latter: in Dirac and Weyl semimetals, parallel electric and magnetic fields can enhance the longitudinal conductivity through charge pumping between nodes of opposite chirality[12;34]. Here, the angular maps are used to characterize the competition between transverse orbital MR and longitudinal suppression, rather than to identify a unique microscopic mechanism.

The temperature evolution shown in Fig. 4 establishes the regime in which the angular contrast is strongest. At 13 T, the low-temperature profiles display sharply defined angular lobes and a strong contrast between the large transverse MR and the suppressed response near the longitudinal configuration. As temperature increases, the anisotropic pattern broadens and the overall MR magnitude decreases substantially. This thermal weakening is consistent with the reduction of carrier mobility and the increasing importance of scattering in the multiband system[10;19;34]. The rapid degradation of the angular anisotropy above approximately 50 K is particularly notable, since it coincides with the temperature range where the Hall response and effective multicarrier parameters evolve most strongly. These observations link the angular contrast to the same temperature-dependent transport weights that shape the XMR state.

Figure 5 further demonstrates that the angular MR anisotropy is strongly field dependent at $T = 2$ K. At low magnetic fields, the polar profiles are relatively smooth and the contrast be-

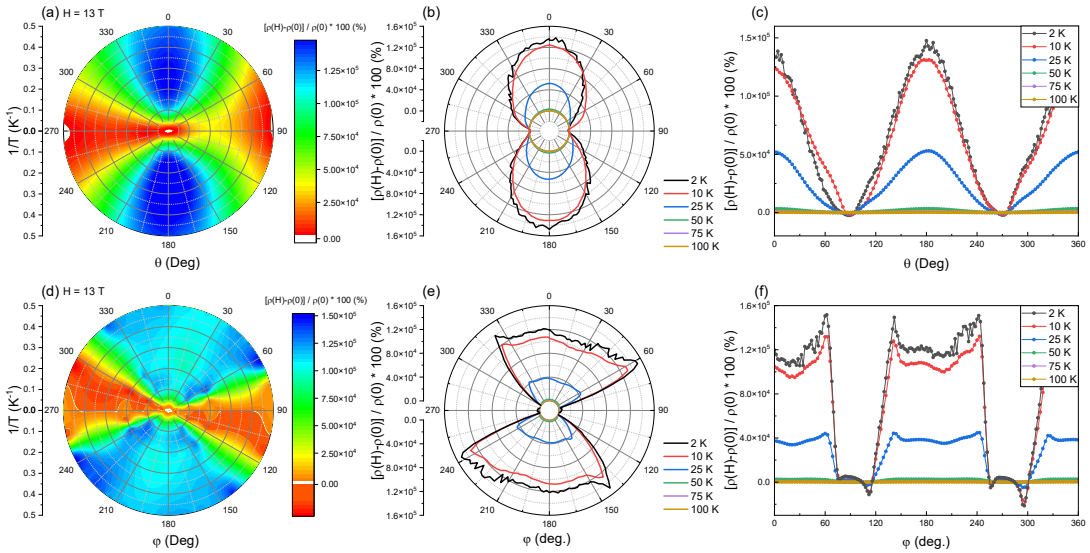

Fig. 4. Temperature evolution of the angular magnetoresistance at $B = 13$ T for the θ rotation (a–c) and ϕ rotation (d–f). (a),(d) Polar color maps: the azimuthal coordinate is the rotation angle, the radial coordinate is inverse temperature $1/T$ (K^{-1}), and color represents MR in percent. (b),(e) Polar MR curves, with radial coordinate MR, at $T = 2$, 10, 25, 50, 75, and 100 K. (c),(f) The corresponding MR curves plotted against angle in Cartesian coordinates at the same temperatures. Rotation geometries are defined in Fig. 3(a).

tween transverse and longitudinal configurations is weak. As the field increases, both the transverse positive MR and the angular contrast grow rapidly. The contour representation shows that the longitudinal suppression develops continuously over an angular interval around $\mathbf{B} \parallel \mathbf{J}$. This evolution emphasizes the role of the anisotropic orbital response and field-dependent transport weights. A chiral-anomaly-related longitudinal correction remains a possible contribution within the framework described above[12].

At low temperature and high field, the θ profiles exhibit a prominent two-lobed pattern, whereas the ϕ profiles contain additional angular structure. This dependence on the rotation plane is consistent with anisotropic orbital transport in LaSb, where elongated X-centered electron pockets are established[2;19]. The absolute MR magnitude and angular contrast both diminish on warming or reducing the field.

The reduction of the absolute angular MR contrast above approximately 50 K accompanies the rapid evolution of the Hall response and the clearer separation of the finite-field normalized resistivity curves in Fig. 1(d). This correspondence suggests a redistribution of the effective transport contributions from different Fermi pockets. A Lifshitz-like crossover remains a possible interpretation, although establishing an actual change in Fermi-surface connectivity would require temperature-dependent quantum-oscillation or electronic-structure measurements. More generally, the observations are consistent with a progressive reduction of highly anisotropic high-mobility contributions at elevated temperature. The ADMR results therefore support the view that the XMR state in LaSb involves multiple pockets with distinct geometrical

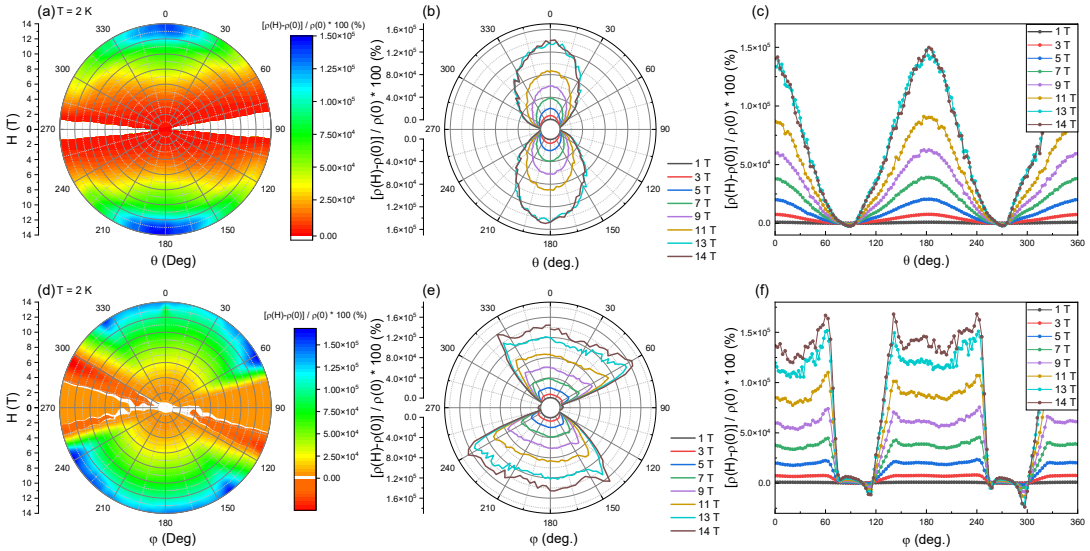

Fig. 5. Field evolution of the angular magnetoresistance at $T = 2$ K for the θ rotation (a–c) and ϕ rotation (d–f). (a),(d) Polar color maps: the azimuthal coordinate is the rotation angle, the radial coordinate is magnetic field (T), and color represents MR in percent. (b),(e) Polar MR curves, with radial coordinate MR, at $B = 1$, 3, 5, 7, 9, 11, 13, and 14 T. (c),(f) The corresponding MR curves plotted against angle in Cartesian coordinates at the same fields. Rotation geometries are defined in Fig. 3(a).

and transport characteristics.

The combined temperature and field dependence of Figs. 4 and 5 therefore establishes a strongly anisotropic magnetotransport regime at low temperature and high field. Its dominant transverse response is consistent with high-mobility compensated carriers, while the pronounced longitudinal suppression motivates consideration of additional orientation-dependent contributions. These observations place possible chiral-anomaly-related transport in the context of the compensated multiband background without using the angular maps as a standalone identification of that mechanism.

3.3 Quantum oscillations and Fermi-surface topology

To investigate the Fermi-surface orbits contributing to the low-temperature response, we performed high-field magnetotransport and magnetization measurements at 2 K. As shown in Fig. 6, clear Shubnikov–de Haas (SdH) oscillations are observed in the longitudinal and Hall transport channels, and de Haas–van Alphen (dHvA) oscillations are also resolved in the magnetic signal. Their periodicity in $1/B$ is characteristic of Landau quantization of closed cyclotron orbits. The combined transport and thermodynamic measurements support a bulk-pocket interpretation when considered together with the established three-dimensional Fermi surface of LaSb[2;19]; their coexistence alone does not determine the dimensionality of every oscillatory contribution.

Figure 6(a) shows the field-dependent longitudinal resistivity signal and the second-derivative representation of its background-subtracted oscillatory component. The longitudinal signal contains the large positive magnetoresistance background of the high-mobility compensated state, upon which oscillatory modulations become increasingly visible at high field. The oscillatory component is obtained by subtracting a smooth field-dependent background, and the second-derivative treatment enhances the extrema. The growth of oscillation amplitude with field is consistent with increasing Landau-level separation, so that thermal and disorder broadening become less important relative to this separation[36]. The resolved oscillations indicate that disorder broadening is sufficiently small to permit quantization; the associated damping concerns the quantum lifetime, rather than providing a direct measurement of the transport lifetime.

Figure 6(b) presents the Hall resistivity together with the corresponding second-derivative representation of the oscillatory contribution isolated by smooth-background subtraction. The Hall response weights electron- and hole-like carriers differently from the longitudinal channel. Resolving oscillations in both channels therefore provides complementary information about the quantized electronic states involved in transport. The derivative representation also sharpens the field-dependent oscillatory features.

Figure 6(c) shows the background-subtracted dHvA signal as a function of inverse magnetic field, $1/B$. In contrast to transport measurements, which depend on the scattering-weighted conductivity of mobile carriers, the dHvA effect probes the oscillatory thermodynamic response. It thus supplies an independent probe of Landau quantization and the basis for the frequency analysis in Fig. 7. The relation between an oscillation frequency and an extremal orbit area is given by the Onsager relation,

$$F = \frac{\hbar}{2\pi e} A_{\mathrm{F}}, \tag{1}$$

where F is the oscillation frequency and A_{F} is the extremal cross-sectional area perpendicular to the applied field. Interpreting these areas in the established LaSb Fermi-surface framework provides the pocket assignments discussed below.

Taken together, the longitudinal and Hall SdH oscillations and the magnetic dHvA oscillations provide complementary transport and thermodynamic evidence for well-resolved cyclotron orbits in LaSb. They supply the experimental basis for comparing the principal frequencies with the known bulk Fermi surface and for analyzing orbit-dependent phase offsets. This connects the quantum-oscillation results with the multiband electronic structure underlying the magnetotransport response.

The fast Fourier transform (FFT) spectrum shown in Fig. 7(a) displays three principal frequency branches: $F_\alpha \approx 215.77$ T, $F_\beta \approx 451.15$ T, and $F_\gamma \approx 882.7$ T, together with features labeled 2α and 3α. The quoted values are FFT peak positions; the β-branch slope from the Landau-fan fit

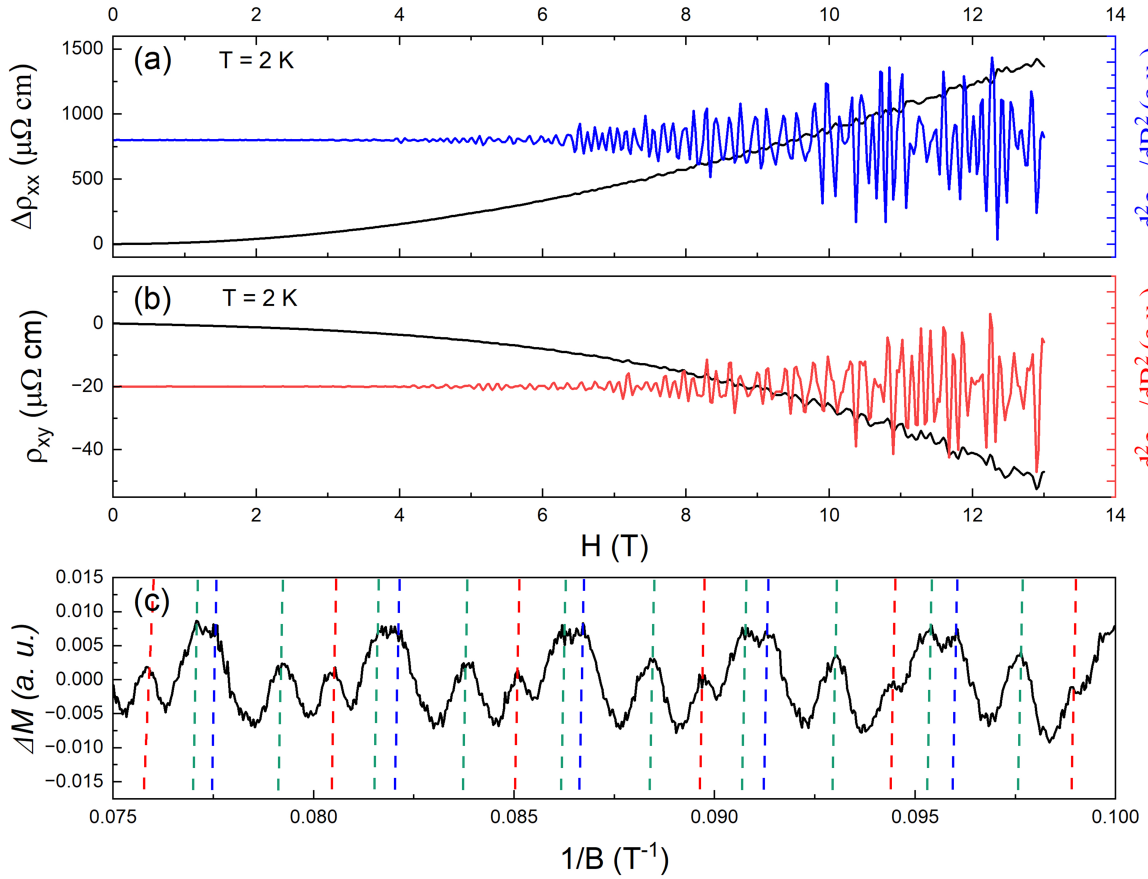

Fig. 6. Quantum-oscillation signals at $T = 2$ K. (a) Longitudinal resistivity signal, labeled $\Delta\rho_{xx}$ in the plot (black, left axis), and the second-derivative representation of its background-subtracted SdH component (blue, right axis). (b) Hall resistivity (black, left axis) and the corresponding second-derivative SdH signal (red, right axis). The derivative traces are labeled $-\mathrm{d}^2\rho_{xx}/\mathrm{d}B^2$ and $-\mathrm{d}^2\rho_{xy}/\mathrm{d}B^2$ and are shown in arbitrary units. (c) Background-subtracted dHvA signal $\Delta M_{\mathrm{osc}} = M - M_{\mathrm{bg}}$ versus inverse magnetic field over the approximately 10.0–13.3 T interval used for the fan analysis. Colored dashed guides mark selected oscillatory features. A smooth field-dependent background was removed when isolating the oscillatory components.

is approximately 451.72 T and is a separate frequency estimate.

We use the pocket-family nomenclature of Han et al.[19]: α denotes the ellipsoidal electron-pocket family centered at X, while β and γ denote the smaller and larger hole pockets centered at Γ, respectively. This one-electron-family/two-hole-pocket structure is also supported by ARPES and band calculations[2;20;31]. The labels are not universal: Zeng et al. label the larger Γ-centered hole sheet δ, whereas their γ denotes another extremal cross-section of the X-centered electron family[2]. The assignments here are therefore literature-guided pocket correspondences for the phase analysis, rather than carrier identities determined by the frequencies alone. The three branches denote principal orbit families, not a count of all symmetry-equivalent pockets in the Brillouin zone.

We next analyze the topological character of these pockets using Landau-level fan diagrams. For a three-dimensional Fermi surface, the oscillation phase can be expressed as

$$n = \frac{F}{B} - \frac{1}{2} + \delta + \frac{\phi_B}{2\pi}, \tag{2}$$

where n is the Landau index, $\delta = \pm 1/8$ is the additional phase shift for a three-dimensional orbit, and ϕ_B is the Berry phase. In this representation, the intercept obtained by extrapolating n to $1/B \to 0$ provides information on the phase offset and hence on the topological character of the corresponding orbit.

Landau-level indexing was performed for the clearly resolved oscillation extrema in the high-field interval of approximately 10–13 T, using the same indexing convention for all three branches. The Landau-fan fits and indexing convention are summarized in Fig. S2 and the accompanying Supplementary text; Table S2 gives the γ-orbit intercept under the original and integer-shifted index labels. As shown in Fig. 7(b)–7(d), the fitted central intercepts are $b_\alpha = 0.397$, $b_\beta = 0.270$, and $b_\gamma = 0.980$. The α electron orbit and β hole orbit have central offsets compatible with trivial-phase expectations under the adopted convention. These are phase-compatibility statements and do not uniquely classify either pocket.

For the γ branch, the fitted intercept is $b_\gamma = 0.980 \pm 0.071$ (reported standard error), with a reported 95% confidence interval of $[0.754, 1.206]$. A uniform shift of all Landau indices by one changes the intercept by an integer without changing its phase class. The centered representation is therefore $b'_\gamma = b_\gamma - 1 = -0.020$, with the confidence interval $[-0.246, 0.206]$. Under Eq. (2), this interval contains the ideal three-dimensional nontrivial offsets $\pm 1/8$ and excludes the nominal trivial offsets $\pm 3/8$, all expressed in the same centered modulo-one convention. We interpret this as a phase signature compatible with a nontrivial Berry-phase contribution on the assigned γ orbit. The interpretation depends on the adopted indexing and three-dimensional phase correction and does not by itself establish a global band-topological invariant. Together with the α and β results, it motivates a pocket-dependent phase description of LaSb[28–30;37;38].

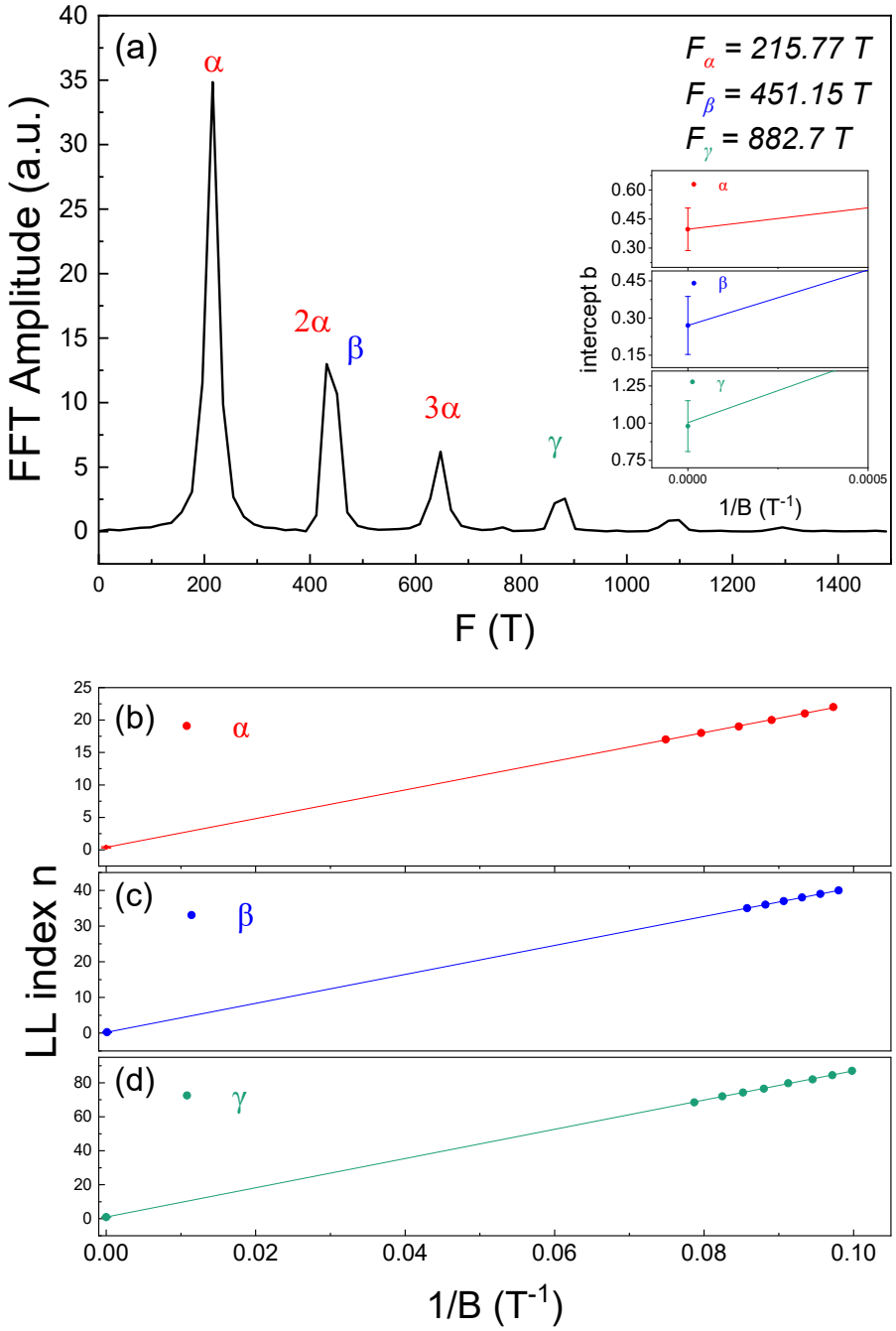

Fig. 7. (a) FFT spectrum of the background-subtracted dHvA signal, with principal peaks $F_\alpha = 215.77$ T, $F_\beta = 451.15$ T, and $F_\gamma = 882.7$ T, and harmonic features labeled 2α and 3α. The inset enlarges the fitted intercepts of the three Landau fans; error bars denote the reported standard errors. (b–d) Landau-fan diagrams for the α, β, and γ branches, respectively, with linear fits $n = F/B + b$ and intercepts $b_\alpha = 0.397$, $b_\beta = 0.270$, and $b_\gamma = 0.980$. Symbols at $1/B = 0$ mark extrapolated intercepts rather than measured extrema. The dHvA indexing convention is specified in Fig. S2 and the accompanying Supplementary text. Pocket labels follow the literature-guided correspondence described in the main text.

3.4 Multicarrier conductivity analysis

To connect the pocket-resolved quantum-oscillation results with the measured transport response, we simultaneously fitted the longitudinal and Hall conductivities using a semiclassical multicarrier Drude model with the number of effective conducting channels $N_C = 2$–5:

$$\sigma_{xx}(B) = \sum_{i=1}^{N_C} \frac{n_i e \mu_i}{1 + (\mu_i B)^2}, \tag{3}$$

$$\sigma_{xy}(B) = \sum_{i=1}^{N_C} s_i \frac{n_i e \mu_i^2 B}{1 + (\mu_i B)^2}, \tag{4}$$

where n_i, μ_i, and s_i denote the carrier density, mobility, and carrier sign of the ith channel, respectively. Here ρ_{xy} denotes the off-diagonal tensor element E_x/J_y, with $\rho_{yx} = -\rho_{xy}$; the coefficients s_i are -1 for electrons and $+1$ for holes. The conductivity components were obtained from the measured resistivity tensor using

$$\sigma_{xx}(B) = \frac{\rho_{xx}(B)}{\rho_{xx}^2(B) + \rho_{xy}^2(B)}, \tag{5}$$

$$\sigma_{xy}(B) = -\frac{\rho_{xy}(B)}{\rho_{xx}^2(B) + \rho_{xy}^2(B)}. \tag{6}$$

The fitting results are summarized in Fig. 8. Within the low-field interval displayed in Fig. 8, a two-channel model captures the broad trends but does not fully reproduce the detailed field dependence of the longitudinal and Hall conductivities. As the number of effective channels is increased, the agreement improves systematically, as evidenced by the decreasing mean-square fitting error in the inset of Fig. 8(b) and the reduced residuals in Fig. 8(c),(d). The residuals are displayed in percent. This improvement shows that additional effective mobility components provide a more flexible description of the measured low-temperature field dependence.

The improvement obtained by adding effective transport components should not be interpreted as a unique determination of their number or as evidence for a corresponding number of distinct Fermi pockets. Quantum oscillations identify the principal extremal bulk orbits in momentum space, whereas conductivity fitting reflects how different carriers contribute to the field-dependent transport response. In practice, anisotropic pockets, symmetry-related valleys, mobility distributions, and pocket-dependent scattering rates can cause one nominal Fermi pocket to manifest as more than one effective Drude component in transport analysis[39–42].

Taken together, the nonlinear Hall response, anisotropic magnetoresistance, quantum-oscillation frequencies, phase analysis, and multicarrier conductivity fitting support a compensated yet electronically complex multiband state in LaSb. The two-band model provides effective parameters for the overall temperature evolution (Fig. 2(c)), while additional Drude

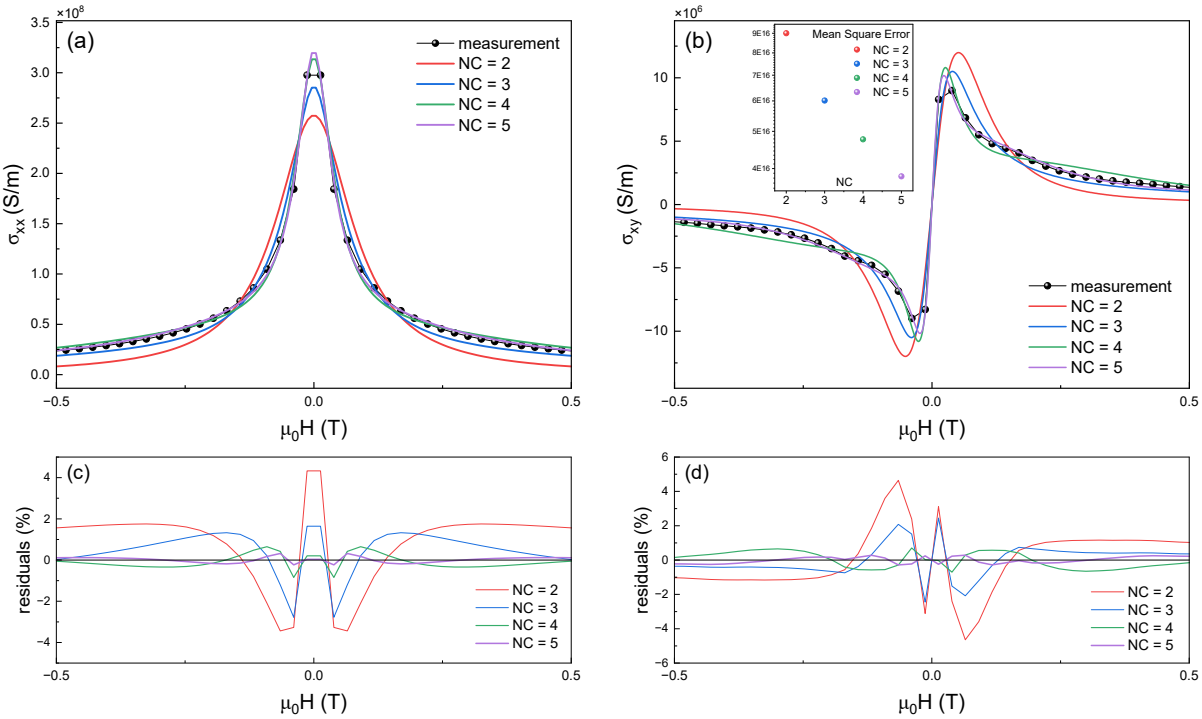

Fig. 8. Low-field multicarrier Drude fits with $N_C = 2$–5 to (a) longitudinal conductivity σ_{xx} and (b) Hall conductivity σ_{xy} over the displayed interval $-0.5\ \mathrm{T} \leq \mu_0 H \leq 0.5\ \mathrm{T}$. Black symbols represent measurements; red, blue, green, and purple curves correspond to $N_C = 2$, 3, 4, and 5, respectively. (c),(d) Corresponding longitudinal- and Hall-conductivity residuals, expressed in percent. The inset in (b) shows the mean-square fitting error versus N_C. The effective channel count parameterizes the transport response and is not a direct count of distinct Fermi pockets.

components improve the description of the detailed field dependence. The XMR is consistent with the combined effects of high mobility, near charge compensation, and anisotropic orbital transport. The pocket-dependent phase signatures add information on the quantized electronic states without requiring topology to be the dominant cause of XMR. The correlated temperature evolution of the Hall signal, resistivity plateau, and ADMR points to changing transport weights, with a Lifshitz-like crossover retained as a possible electronic-structure interpretation.

4 Conclusion

We have investigated the extreme magnetoresistance of high-quality LaSb single crystals through combined magnetotransport and quantum-oscillation measurements. The transport data reveal a compensated multiband state characterized by a field-induced resistivity upturn, a low-temperature plateau, a nonlinear Hall response, and strong angular magnetoresistance anisotropy. Additional effective Drude components improve the conductivity fits beyond the minimal two-carrier description, highlighting the importance of distinct mobility and transport weights even near overall electron–hole compensation.

The three principal quantum-oscillation branches are assigned, using established LaSb Fermi-surface correspondence, to the α electron-pocket family and the β and γ hole pockets. Landau-fan analysis yields distinct pocket-dependent phase signatures: the α and β orbits are compatible with trivial-phase expectations, whereas the γ orbit is compatible with a nontrivial Berry-phase contribution under the adopted three-dimensional convention. This orbit-resolved interpretation is consistent with the multiband transport framework without equating a fan intercept with the global band topology.

These results support an XMR state governed primarily by near charge compensation, high mobility, and anisotropic multiband transport. The correlated evolution of resistivity, Hall response, and angular magnetoresistance indicates a temperature-dependent redistribution of transport weights; a Lifshitz-like crossover remains a hypothesis for its electronic-structure origin. LaSb thus provides a useful platform for examining how pocket-dependent phase character and carrier dynamics coexist in an extreme-magnetoresistance semimetal.

Acknowledgements

This work was supported by the Korea Planning & Evaluation Institute of Industrial Technology, Ministry of Trade, Industry and Energy (RS-2025-07322968).

Data Availability

The data are available from the corresponding author upon reasonable request.

Competing Interests

The authors declare no competing interests.

References

1. Tafti, F. F., Gibson, Q. D., Kushwaha, S. K., Haldolaarachchige, N. & Cava, R. J. Resistivity plateau and extreme magnetoresistance in LaSb. *Nat. Phys.* **12**, 272–277 (2016).
2. Zeng, L. K. *et al.* Compensated semimetal LaSb with unsaturated magnetoresistance. *Phys. Rev. Lett.* **117**, 127204 (2016).
3. Ali, M. N. *et al.* Large, non-saturating magnetoresistance in WTe_2. *Nature* **514**, 205–208 (2014).
4. Yan, B. & Felser, C. Topological materials: Weyl semimetals. *Annu. Rev. Condens. Matter Phys.* **8**, 337–354 (2017).
5. Ali, M. N. *et al.* Correlation of crystal quality and extreme magnetoresistance of WTe_2. *Europhys. Lett.* **110**, 67002 (2015).
6. Shekhar, C. *et al.* Extremely large magnetoresistance and ultrahigh mobility in the topological Weyl semimetal candidate NbP. *Nat. Phys.* **11**, 645–649 (2015).
7. Huang, X. *et al.* Observation of the chiral-anomaly-induced negative magnetoresistance in 3D Weyl semimetal TaAs. *Phys. Rev. X* **5**, 031023 (2015).
8. Armitage, N. P., Mele, E. J. & Vishwanath, A. Weyl and Dirac semimetals in three-dimensional solids. *Rev. Mod. Phys.* **90**, 015001 (2018).
9. Burkov, A. A. Weyl metals. *Annu. Rev. Condens. Matter Phys.* **9**, 359–378 (2018).
10. Liang, T. *et al.* Ultrahigh mobility and giant magnetoresistance in the Dirac semimetal Cd_3As_2. *Nat. Mater.* **14**, 280–284 (2015).
11. Lv, B. Q. *et al.* Experimental discovery of Weyl semimetal TaAs. *Phys. Rev. X* **5**, 031013 (2015).
12. Zhang, C. L. *et al.* Signatures of the Adler–Bell–Jackiw chiral anomaly in a Weyl fermion semimetal. *Nat. Commun.* **7**, 10735 (2016).

13. Wang, Z., Weng, H., Wu, Q., Dai, X. & Fang, Z. Three-dimensional Dirac semimetal and quantum transport in Cd_3As_2. *Phys. Rev. B* **88**, 125427 (2013).

14. Lv, B. Q. *et al.* Observation of Weyl nodes in TaAs. *Nat. Phys.* **11**, 724–727 (2015).

15. Cao, J. *et al.* Landau level splitting in Cd_3As_2 under high magnetic fields. *Nat. Commun.* **6**, 7779 (2015).

16. Weng, H., Fang, C., Fang, Z., Bernevig, B. A. & Dai, X. Weyl semimetal phase in noncentrosymmetric transition-metal monophosphides. *Phys. Rev. X* **5**, 011029 (2015).

17. Khalid, S. & Janotti, A. Trivial to nontrivial topology transition in rare-earth pnictides with epitaxial strain. *Phys. Rev. B* **102**, 035151 (2020).

18. Sun, S., Wang, Q., Guo, P. J., Liu, K. & Lei, H. Large magnetoresistance in LaBi: Origin of field-induced resistivity upturn and plateau in compensated semimetals. *New J. Phys.* **18**, 082002 (2016).

19. Han, F. *et al.* Separation of electron and hole dynamics in the semimetal LaSb. *Phys. Rev. B* **96**, 125112 (2017).

20. Guo, P. J., Yang, H. C., Zhang, B. J., Liu, K. & Lu, Z. Y. Charge compensation in extremely large magnetoresistance materials LaSb and LaBi revealed by first-principles calculations. *Phys. Rev. B* **93**, 235142 (2016).

21. Thoutam, L. R. *et al.* Temperature-dependent three-dimensional anisotropy of the magnetoresistance in WTe_2. *Phys. Rev. Lett.* **115**, 046602 (2015).

22. Kumar, N. *et al.* Observation of pseudo-two-dimensional electron transport in the rock salt-type topological semimetal LaBi. *Phys. Rev. B* **93**, 241106(R) (2016).

23. Yuan, Z., Lu, H., Liu, Y., Wang, J. & Jia, S. Large magnetoresistance in compensated semimetals $TaAs_2$ and $NbAs_2$. *Phys. Rev. B* **93**, 184405 (2016).

24. Zhao, Y. *et al.* Anisotropic Fermi surface and quantum limit transport in high mobility three-dimensional Dirac Semimetal Cd_3As_2. *Phys. Rev. X* **5**, 031037 (2015).

25. Xu, J. *et al.* Origin of the extremely large magnetoresistance in the semimetal YSb. *Phys. Rev. B* **96**, 075159 (2017).

26. Singha, R., Pariari, A. K., Satpati, B. & Mandal, P. Large nonsaturating magnetoresistance

and signature of nondegenerate Dirac nodes in ZrSiS. *Proc. Natl. Acad. Sci. U.S.A.* **114**, 2468–2473 (2017).

27. Shen, B., Deng, X., Kotliar, G. & Ni, N. Fermi surface topology and negative longitudinal magnetoresistance observed in the semimetal $NbAs_2$. *Phys. Rev. B* **93**, 195119 (2016).

28. Niu, X. H. *et al.* Presence of exotic electronic surface states in LaBi and LaSb. *Phys. Rev. B* **94**, 165163 (2016).

29. Oinuma, H. *et al.* Three-dimensional band structure of LaSb and CeSb: Absence of band inversion. *Phys. Rev. B* **96**, 041120(R) (2017).

30. Dey, U., Chakraborty, M., Taraphder, A. & Tewari, S. Bulk band inversion and surface Dirac cones in LaSb and LaBi: Prediction of a new topological heterostructure. *Sci. Rep.* **8**, 14867 (2018).

31. Kumigashira, H. *et al.* High-resolution angle-resolved photoemission study of LaSb. *Phys. Rev. B* **58**, 7675–7680 (1998).

32. Wang, K., Graf, D., Li, L., Wang, L. & Petrovic, C. Anisotropic giant magnetoresistance in $NbSb_2$. *Sci. Rep.* **4**, 7328 (2014).

33. Parish, M. M. & Littlewood, P. B. Non-saturating magnetoresistance in heavily disordered semiconductors. *Nature* **426**, 162–165 (2003).

34. Lu, H.-Z. & Shen, S.-Q. Quantum transport in topological semimetals under magnetic fields. *Front. Phys.* **12**, 127201 (2017).

35. Schumann, T., Goyal, M., Kealhofer, D. A. & Stemmer, S. Negative magnetoresistance due to conductivity fluctuations in films of the topological semimetal Cd_3As_2. *Phys. Rev. B* **95**, 241113(R) (2017).

36. Shoenberg, D. *Magnetic Oscillations in Metals* (Cambridge University Press, Cambridge, 1984).

37. Mikitik, G. P. & Sharlai, Yu. V. Manifestation of Berry's phase in metal physics. *Phys. Rev. Lett.* **82**, 2147–2150 (1999).

38. Taskin, A. A. & Ando, Y. Berry phase of nonideal Dirac fermions in topological insulators. *Phys. Rev. B* **84**, 035301 (2011).

39. Pavlosiuk, O., Swatek, P., Kaczorowski, D. & Wiśniewski, P. Magnetoresistance in LuBi and YBi semimetals due to nearly perfect carrier compensation. *Phys. Rev. B* **97**, 235132 (2018).

40. Kim, H.-J. *et al.* Dirac versus Weyl fermions in topological insulators: Adler-Bell-Jackiw anomaly in transport phenomena. *Phys. Rev. Lett.* **111**, 246603 (2013).

41. Hu, J. & Rosenbaum, T. F. Classical and quantum routes to linear magnetoresistance. *Nat. Mater.* **7**, 697–700 (2008).

42. Pippard, A. B. *Magnetoresistance in Metals* (Cambridge University Press, Cambridge, 1989).

Supplementary Files

This is a list of supplementary files associated with this preprint. Click to download.

- SILaSbNPGasiamaterials.docx